

Effects of orbital ellipticity on collisional disruptions of rubble-pile asteroids

Yun Zhang¹ · Hexi Baoyin¹ · Junfeng Li¹ · Derek C. Richardson² · Stephen R. Schwartz³

Received: 10 March 2015 / Accepted: 12 October 2015 / Published online: 29 October 2015
© Springer Science+Business Media Dordrecht 2015

Abstract The behavior of debris ejected from asteroids after collisional disruptions has significant implications for asteroid evolution. Analytical approximations of the elliptic restricted three-body system show that the behavior of ejecta varies significantly with the orbital eccentricity and true anomaly of an asteroid. To study these orbital perturbative effects on collision outcomes, we conduct a series of low-speed collision simulations using a combination of an N -body gravity algorithm and the soft-sphere discrete element method. The asteroid is modeled as a gravitational aggregate, which is one of the plausible structures for asteroids whose sizes are larger than several hundreds of meters. To reduce the effect of complicating factors raised by the mutual interaction between post-collision fragments on the outcomes, a low-resolution model and a set of frictionless material parameters are used in the first step of exploration. The results indicate that orbital perturbations on ejecta arising from the eccentricity and true anomaly of the target asteroid at the time of impact cause larger mass loss and lower the catastrophic disruption threshold (the specific energy required to disperse half the total system mass) in collision events. The “universal law” of catastrophic disruption derived by Stewart and Leinhardt (Astrophys. J. Lett. 691:L133–L137, 2009) can be applied to describe the collision outcomes of asteroids on elliptical heliocentric orbits. Through analyses of ejecta velocity distributions, we

develop a semi-analytic description of escape speed from the asteroid’s surface in an elliptic restricted three-body system and show that resulting perturbations have long-term orbital effects on ejecta and can also have an indirect influence on the velocity field of post-fragments through interparticle collisions. Further exploration with a high-resolution model shows that the long-term perturbative effects systematically increase mass loss, regardless of the target’s material parameters and internal configuration, while indirect effect on mass loss is much more complicated and is enhanced when a coarse material or high-porosity model is used.

Keywords Celestial mechanics · Methods: numerical · Minor planets, asteroids: general · Planets and satellites: physical evolution

1 Introduction

Collisions are crucial and common in the Solar System. The behavior of debris ejected from asteroids because of collisions has significant implications for the evolution of asteroids and the formation of satellites in the early Solar System. In addition, because some Earth-crossing asteroids pose threats to the Earth, and the kinetic impact method is considered to be a relatively feasible and efficient technique (Sanchez et al. 2009), characterizing the outcomes in asteroid impacts is important for designing a successful asteroid defense mission.

Because of the lack of observations and laboratory studies, numerical simulations are widely used to infer the details of collisions of asteroids (e.g., Leinhardt et al. 2000). Previous simulation studies indicate that the outcome of a collision is dependent on the impact conditions (e.g., impact velocity, impact angle, and projectile-to-target mass ratio; see Leinhardt and Stewart 2012), the pre-impact rotation

✉ H. Baoyin
baoyin@tsinghua.edu.cn

¹ School of Aerospace Engineering, Tsinghua University, Beijing 100084, People’s Republic of China

² Department of Astronomy, University of Maryland, College Park, MD 20740-2421, United States

³ Lagrange Laboratory, University of Nice Sophia Antipolis, CNRS, Observatoire de la Côte d’Azur, C.S. 34229, 06304 Nice Cedex 4, France

rate of the target (Ballouz et al. 2014), the internal structure (Asphaug et al. 1998; Jutzi and Michel 2014) and the material properties (Ballouz et al. 2015), which significantly improved our understanding of the diversity of collision outcomes. However, these studies treated the target as an isolated body without considering the effect of the asteroid's orbit on the collisional evolution.

Observations and numerical results indicate that most main-belt asteroids follow non-circular orbits (Jedicke and Metcalfe 1998), and in general, the orbits of near-Earth asteroids have relatively high eccentricity (Bottke et al. 2002). Thus, the asteroid ejecta from an impact event can be treated as the third small body in an elliptic restricted three-body problem (ERTBP). In this system, the Hill's region, where the asteroid's gravity dominates over solar tides, depends on the orbital position of the asteroid (Makó and SzeKovits 2004; Voyatzis et al. 2012). Previous research has shown that nonzero heliocentric eccentricity will dramatically narrow the orbital stability zones around small Solar System bodies (e.g., Hamilton and Burns 1992; Richter and Keller 1995). Therefore, noncircular orbits can be supposed to have significant influence on the outcomes of rubble-pile collisions.

In this study, the dependence of collision outcomes and the motion of ejecta on the orbital position of impact and the orbital eccentricity of target asteroids is investigated. An elliptic restricted three-body system is studied, and the perturbative effects on the evolution of asteroid ejecta during impact events are analyzed. To confirm the analyses, numerical experiments are conducted to model the impact process.

In order to accurately simulate the collisional dynamics in the presence of the Sun's gravity, a combination of an N -body gravity algorithm and the soft-sphere discrete element method (SSDEM) is applied (Schwartz et al. 2012). In this method, the asteroid is modeled as a gravitational aggregate, which is one of the plausible structures for asteroids whose sizes are larger than several hundreds of meters (Richardson et al. 2002). Because our implementation of SSDEM treats the collision process as a series of linear-spring dashpot contact actions (Cundall and Strack 1979), the method is only suited to study subsonic-speed impacts, where no irreversible damage occurs. Therefore, the impact speed used in our simulations is no more than tens of m/s. Although, in reality, the collisions often occur at supersonic speeds (Michel et al. 2004), the application of subsonic speeds does not prevent us from analyzing the effect of an elliptical orbit on the motion of post-collision fragments. Furthermore, subsonic-speed impacts are expected to have occurred during the planetesimal growth phase during the formation of the solar system (e.g., Lissauer 1993).

We use km-size asteroids in this study since the transition from the strength to the gravity regime is thought to be around 100 m in radius (Stewart and Leinhardt 2009).

The km-size asteroids are more likely to be dominated by self-gravity rather than material strength, so that the model of gravitational aggregates can be regarded as a reasonable proxy for this specific asteroid size. Furthermore, the impact energy required to disperse half the total mass increases with increasing target size in the gravity regime (Benz and Asphaug 1999). Using km-size targets allows us to simulate the catastrophic disruption collisions with SSDEM, where the corresponding impact speeds do not exceed the sound speed of the material.

The outcomes of collisions are described by the mass of the largest post-collision remnant, m_{lr} , and the catastrophic disruption threshold, Q_D^* , which is the specific impact energy required to disperse half the total system mass. We compare our simulation results to the mass-loss equation derived by Stewart and Leinhardt (2009). Furthermore, we derive an analytical approximation of the escape speed from the surface of an asteroid in the ERTBP, which defines the range of the escape ejecta, and use it to infer the mass loss of collisions for the rubble piles in heliocentric orbits.

This paper is organized as follows. Section 2 derives the force analyses of the ejecta in the elliptic restricted three-body system. Section 3 details the numerical method and the model used in this study. Section 4 presents the simulation results. Section 5 analyzes the catastrophic disruption threshold and ejecta velocity distribution of the results, and formulates a description of the escape speed in the ERTBP. Section 6 discusses the implications for collisional evolution in heliocentric orbits. Section 7 presents conclusions.

2 Force analyses of a third body in the ERTBP

Considering an elliptic restricted three-body system, an asteroid moves around the Sun at a non-uniform angular rate that can be described by the first-order time derivative of the true anomaly f :

$$\dot{f} = \sqrt{Gm_{\text{Sun}}(1 + e \cos f)/R^3}, \quad (1)$$

where G is the gravitational constant, m_{Sun} is the mass of the Sun, R is the instantaneous distance from the Sun to the asteroid, which is given by $R = a(1 - e^2)/(1 + e \cos f)$, and a and e are the semi-major axis and eccentricity of the orbit of the asteroid, respectively.

To study the motion of a third body in the ERTBP, application of a non-uniformly rotating and pulsating coordinate system that is centered on the asteroid and rotates with the variable angular velocity is convenient (e.g., Gong and Li 2015). In such a frame, the x axis points to the asteroid, the z axis is along the direction of the angular momentum of the orbit of the asteroid, and the y axis forms a right-handed triad with the x and z axes; the axes have associated unit

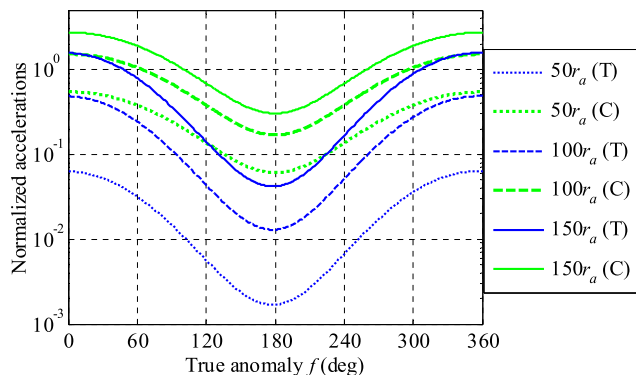


Fig. 1 Normalized accelerations acting on an ejected particle as functions of the true anomaly for $e = 0.5$ at different distances from the asteroid. C denotes the Coriolis acceleration and T denotes the tidal acceleration

vectors \hat{x} , \hat{z} , and \hat{y} , respectively. By linearization, the acceleration $\ddot{\mathbf{r}}$ of a particle moving in the vicinity of the asteroid in the non-uniformly rotating frame can be approximated by

$$\ddot{\mathbf{r}} = -Gm_a \mathbf{r} / r^3 + Gm_{\text{Sun}} / R^3 [(3x\hat{x} - z\hat{z}) + e \cos f (x\hat{x} + y\hat{y}) + 0.5e \sin f (x\hat{y} - y\hat{x}) - 2\dot{f}\hat{z} \times \mathbf{v}], \tag{2}$$

where $\mathbf{r} = r\hat{\mathbf{r}} = x\hat{x} + y\hat{y} + z\hat{z}$ is the position vector of the particle, $\hat{\mathbf{r}}$ is the corresponding unit vector, and \mathbf{v} is the velocity of the particle, which are all measured in the rotating frame. The variable m_a is the mass of the asteroid. According to Eq. (2), the motion of the particle in the vicinity of the asteroid will be acted on by three main external forces: the gravitational attraction of the asteroid, the solar tidal force, and the Coriolis force. The last two forces will generally weaken the gravitational influence of the asteroid.

2.1 The effect of the true anomaly

In one orbital period, the perturbing forces will change with the orbital position of the asteroid. In this study, an asteroid with a mass of 10^{12} kg and a radius, r_a , of 0.6 km is considered as an example case, although the results apply more generally. The semi-major axis a of the asteroid is taken to be 1.75 AU, which is a reasonable value for near-Earth asteroids (Bottke et al. 2002). Figure 1 illustrates the various accelerations acting on an ejected particle as it moves along a radial line away from the asteroid surface at the escape speed. In this case, the asteroid is assumed to be a homogeneous sphere. All accelerations are normalized to the local gravity of the asteroid acting on the ejecta. As shown in Fig. 1, the forces will be enhanced near perihelion mainly because the asteroid–Sun distance R is changing with the true anomaly f and reaches a minimum when $f = 0$.

In addition, the accelerations all act in different directions. In Eq. (2), for the solar tidal force, the first term is

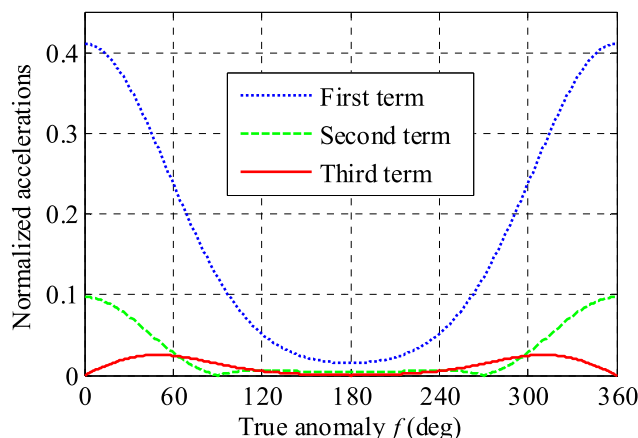


Fig. 2 Magnitudes of three terms in tidal acceleration as functions of the true anomaly for $e = 0.5$ at a distance of $100r_a$

approximately along the direction of the Sun. The term proportional to $e \cos f$ (second term) always aligns parallel or antiparallel to the position vector in the xy coordinate plane, which points toward the asteroid for $f \in (90^\circ, 270^\circ)$ but points toward the opposite direction for $f \in (-90^\circ, 90^\circ)$. The term with $e \sin f$ (third term) is always tangent to the position vector in the xy coordinate plane, and can increase or decrease the speed of an orbiting particle around the asteroid. Figure 2 shows how the magnitudes of the three terms change in one orbital period. The Coriolis term is perpendicular to the orientation of the ejecta velocity at all times. In general, taking into account the magnitudes and directions, the first term and the second term (henceforth, the direct term) in the tidal acceleration will have a major effect on the escaping ejecta, which has a velocity nearly parallel to the position-vector direction.

2.2 The effect of orbital eccentricity

The orbital eccentricity e also has a significant influence on the accelerations, especially when the impact occurs near perihelion. Figure 3 presents the magnitude of these accelerations. The motion path of the ejected particle is the same as that used in Fig. 1. The horizontal axis is measured in units of asteroid radius r_a from the asteroid surface to the boundary of its Hill sphere, the gravitational sphere of influence, the radius of which can be approximately computed to be $r_H = a(m_a/3m_{\text{Sun}})^{1/3}$. Both forces will be enhanced by a larger orbital eccentricity. The tidal forces can even be increased by two orders of magnitude or more for moderately high but still plausible eccentricities. Although the exact values of the accelerations vary, depending on the actual motion path of ejecta and the orbital position of the asteroid, the effect of eccentricity on the accelerations is similar to what is shown in Fig. 3.

After an impact, three different fates are possible for the ejecta: re-impact on the asteroid, become all or part of one

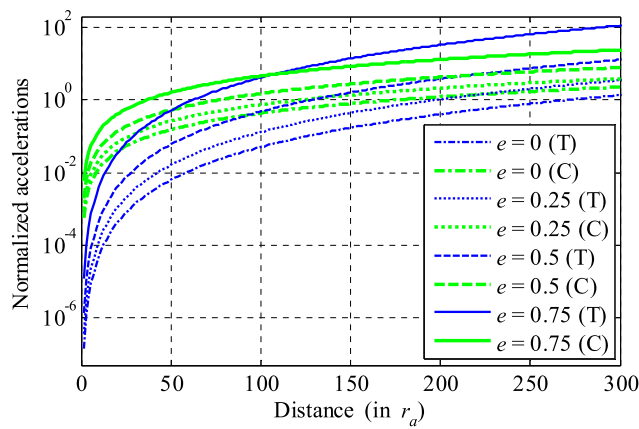


Fig. 3 Various accelerations acting on an ejected particle as functions of distance from the asteroid for different orbital eccentricities at $f = 0^\circ$. All accelerations are normalized to the local gravity of the asteroid acting on the ejecta. *C* denotes the Coriolis acceleration and *T* denotes the tidal acceleration

or more satellites (Durda et al. 2004), or escape, possibly as reaccumulated remnants (Michel et al. 2004). The velocity distribution of the ejected fragments can be described by a continuous probability density function. When the orbital effect is not considered, the boundary of the re-impact outcome and the escape outcome on the ejecta velocity distribution (EVD) curve is the local escape speed of the asteroid. Since the EVD is continuous (see Fig. 9 for an example of displaying the EVD curve), there are some particles whose ejection speed is close to the local escape speed of the asteroid. Thus, a transition zone exists between the re-impact outcome and the escape outcome, where the fates of ejecta are extremely sensitive to the external perturbations (henceforth, the critical ejecta). When the external force slightly changes, the fates of these critical ejecta change. As mentioned above, because of the direct term, the velocity of the ejecta away from the asteroid will be enhanced when the asteroid is near perihelion or weakened near aphelion. Therefore, near perihelion, the energy of the critical ejecta is increased, and it may eventually escape during this time. In this manner, the mass loss will be enhanced. In the subsequent sections, we will conduct a series of numerical experiments to explore the effect of orbital perturbations on the collision process.

3 Numerical method

For the treatment of rubble-pile asteroids, a combination of an N -body gravity algorithm and, more recently, the soft-sphere discrete element method (SSDEM) for computing particle contact forces, is typically used (e.g., Sánchez and Scheeres 2011; Schwartz et al. 2012). In this approach, the asteroid is modeled as a self-gravitational aggregate of

smaller, indestructible spheres. The force acting on each particle is described by

$$\vec{F}_i = \sum_{j=1, j \neq i}^N \vec{F}_{ij}^{(g)} + \sum_{j=1}^{N_c} \vec{F}_{ij}^{(c)}, \tag{3}$$

where N is the total number of particles, $\vec{F}_{ij}^{(g)}$ and $\vec{F}_{ij}^{(c)}$ are the gravitational pull and contact force (if it exists) of particle j on the particle i , and N_c is the coordination number of particle i . When the contact surfaces are not frictionless, the particles in contact can also exhibit resistance to the relative tangential motion of their surfaces, which will also impose a torque on these particles. The motion of particles can be obtained by integrating the force and torque.

We use *pkdgrav*, a parallel N -body gravity tree code originally developed for cosmology (Stadel 2001) and subsequently adapted for handling particle collisions (Richardson et al. 2000, 2011). A soft-sphere model was also implemented in the code (Schwartz et al. 2012). In *pkdgrav*'s soft-sphere implementation, a linear-spring dashpot model is used to describe the normal contact force \vec{F}_n and the tangential sliding resistance \vec{F}_t (Cundall and Strack 1979). In brief, the contact force between two particles is given by

$$\begin{aligned} F_n &= -k_n \xi + C_n u_n, \\ F_t &= \min(k_t D + C_t u_t, \mu_s |F_n|), \end{aligned} \tag{4}$$

which depend on the spring constants, k_n and k_t , and the plastic damping parameters, C_n and C_t (which are related to the normal and tangential coefficients of restitution, ε_n and ε_t). The variable ξ is the mutual compression of these two particles, and D is the total tangential elongation during this collision. The dashpot force is linearly proportional to the normal relative speed and tangential relative speed u_n and u_t . The variable μ_s is the coefficient of static friction. In addition, rolling and twisting resistances were also implemented in *pkdgrav* (Schwartz et al. 2012); with this option, we are able to model a more realistic granular system and investigate the effect of material properties. The effect of these additional friction resistances can be represented by the friction coefficients, μ_r and μ_t , respectively. A second-order leapfrog method is applied to solve the equations of motion. The numerical approach has been validated through comparison with laboratory experiments (e.g., Schwartz et al. 2014) and has been successfully used to study the collision outcomes between rubble-pile asteroids at low speed (Ballouz et al. 2014, 2015).

3.1 Parameter setup

For the simulations presented here, the target is modeled as a gravitational aggregate with total mass $m_{\text{targ}} = 10^{12}$ kg and bulk diameter of ~ 1.2 km (consistent with the model used in Sect. 2). The initial configuration of the aggregate is created

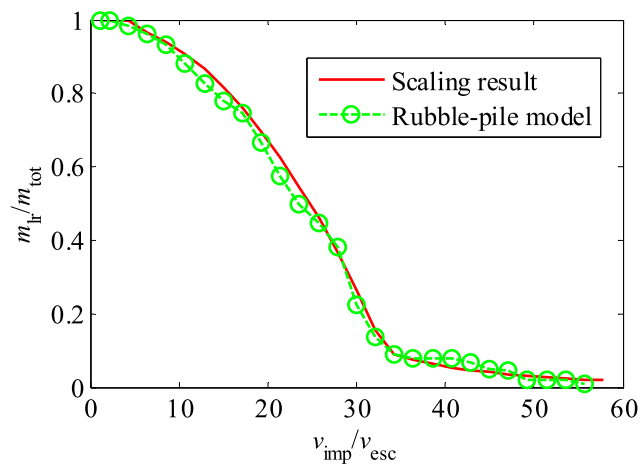


Fig. 4 Mass ratio m_{lr}/m_{tot} for the rubble-pile model and scaling result

by placing spheres randomly in a spherical cloud and allowing the cloud to gravitationally collapse with highly inelastic collisions, which can reduce artificial shear strength arising from the crystalline structure of hexagonal close packing of spheres (Ballouz et al. 2014). Another way to avoid the artificial effect is to use a model consisting of polydisperse particles. In this study, we do not consider the effect of a size distribution of particles, which is outside the scope of this work. To simplify characterization of the ejection velocity of post-collisional ejecta, the projectile is modeled as a single sphere with mass $m_{proj} = 2 \times 10^{10}$ kg and a diameter of 250 m. To ensure that the impact speed and the initial configuration are not influenced by the non-circular orbit, the target and projectile start out nearly in contact for all cases.

Based on hypervelocity impact simulations, Benz and Asphaug (1999) found the transition from the strength to the gravity regime occurs between 100 m and 1000 m in radius; observations (Pravec et al. 2002) also show asteroids smaller than 200 m in diameter can attain fast rotations, implying tensile strength. The recent observations of breakup of the main-belt asteroid P/2013 R3 (Jewitt et al. 2014) show that the asteroid consists of tens of distinct components with various radii (the effective radius of the largest one up to 200 m in radius). Therefore, the main building blocks for rubble piles in the inner Solar System could be as big as a few hundred meters in diameter (Walsh and Richardson 2006). With particles of this size, our target could be constructed from ~ 200 spherical particles (we actually used particles of radius 80 m in our idealized model). As shown in Fig. 4, this model has enough resolution to model collision outcomes. Another important reason for using the low-resolution model is to minimize the effect of mutual interaction between post-collision fragments that would otherwise complicate interpretation. Because self-gravity can lead to gravitational reaccumulation (Michel et al. 2004), ejected fragments cannot be considered massless, particularly in a

Table 1 List of material SSDEM parameters

Parameters	μ_s	μ_r	μ_t	ε_n	ε_t
Smooth	0.0	0.0	0.0	0.8	1.0
Gravel	1.31	3.0	3.0	0.55	0.55

catastrophic event, and this may weaken the signature of orbital perturbations. Compared with a high-resolution model, the post-collision fragments in the low-resolution model are widely spaced, where the occurrence of reaccumulation is infrequent. Nevertheless, we also conduct a series of simulations with a higher number of particles ($N_{targ} = 2896$) to verify that the conclusions we draw from the low-resolution experiments are also applicable for a high-resolution model (see Sect. 6). To ensure there is ample time for the post-collision fragments to reach equilibrium and allow for clear differentiation of ejecta outcomes, the total simulation time is set to one orbital period.

As suggested by Schwartz et al. (2012), the parameters used in the normal contact model can be determined by

$$k_n \sim m \left(\frac{v_{max}}{\xi_{max}} \right)^2, \quad (5)$$

$$C_n \sim -2 \ln \varepsilon_n \sqrt{\frac{k_n \mu}{\pi^2 + (\ln \varepsilon_n)^2}},$$

where m and v_{max} are the mass and maximum expected speed of the most energetic particles in the simulation, ξ_{max} is the maximum of interparticle penetration, which is typically set to 1 % of the smallest particle radius in the simulation; and μ is the reduced mass of the colliding pair. Thus, in our simulation, for which the highest collisional speed ~ 10 m/s, k_n is set to $\sim 2 \times 10^{12}$ kg/s². The tangential spring constant $k_t \sim (2/7)k_n$. Based on the choice of ξ_{max} and k_n , for adequately resolving the contact process, the timestep Δt is set to ~ 4 ms. In order to improve the efficiency, once the distribution of the post-collision fragments and aggregates is well established (the time scale of this process is several tens of dynamical times for the system; the dynamical time is approximately $1/\sqrt{G\rho}$, where ρ is the bulk density of the rubble pile), a larger timestep (~ 40 ms) is applied with the same friction coefficients and coefficient of restitution by adjusting the value of k_n .

Ballouz et al. (2015) found that the mass loss due to collisions is sensitive to the material properties. In fact, the contact mechanics of surfaces associated with non-zero friction coefficients can substantially influence the velocity distribution of particles, and accordingly cause noticeable differences in the collision outcomes. This influence may offset the effect of orbital perturbations. To minimize the effect of particle-particle collisions on the velocity distribution, the particles are modeled as idealized frictionless spheres; i.e., the friction coefficients are set to 0. For this case, the normal

coefficient of restitution ϵ_n is set to 0.8 for rock collisions (Durda et al. 2011). The material parameters are summarized in Table 1 (“smooth”). We also investigate a more realistic set of material parameters in the high-resolution case (see Sect. 6).

3.2 Collision test

To assess the effect of elliptical orbital perturbations on collision outcomes, we compare four different orbital eccentricities for our rubble piles: 0, 0.25, 0.5, and 0.75. For each e , a range of impact speeds is applied to investigate the collision response of the gravitational aggregate to different mass-loss scenarios. This paper focuses on head-on impacts, in which the trajectory of the projectile is directed at the center of the target. Because the level of collisional dissipation will be slightly influenced by the internal configuration of the rubble-pile model (according to Ballouz et al. 2015, the mass-loss deviations is approximately 1 % from the mean) and the initial orientation, a constant rubble-pile configuration (whose porosity is about 0.477) and a fixed relative-impact orientation are used for all simulations. The orientation of the projectile velocity vector is in the reverse direction of the target orbital velocity vector. Before starting the simulations, an understanding of the relation between collision outcomes and impact conditions without considering the orbital effect is necessary. Therefore, we conduct a series of collision tests that serve as nominal collision outcomes.

Figure 4 presents the relation between the mass ratio of the largest post-collision remnant to the total mass of the target plus the projectile m_{lr}/m_{tot} and the normalized impact speed v_{imp}/v_{esc} , where $v_{esc} \sim 0.5$ m/s is the escape speed from the surface of a spherical object with the same total mass and density of 1000 kg/m^3 . The mass of the largest remnant is represented as the sum of its own mass and the mass of materials gravitationally bound to it. To validate the low-resolution model, we compare our results with the scaling laws for head-on impacts in the gravity regime derived by Leinhardt and Stewart (2012):

$$\frac{m_{lr}}{m_{tot}} = \begin{cases} 1, & \text{if } v_{imp} \leq v_{esc} \\ 1 - \frac{5\mu' v_{imp}^2}{16\pi c^* \rho_1 G m_{tot} R_{C1}^2} \left(\frac{1}{4} \frac{(\gamma+1)^2}{\gamma}\right)^{1-2/3\bar{\mu}}, & \\ \text{if } v_{esc} < v_{imp} < v_{supercat}, & \\ \frac{0.1}{1.8^{-1.5}} \left[\frac{5\mu' v_{imp}^2}{8\pi c^* \rho_1 G m_{tot} R_{C1}^2} \left(\frac{1}{4} \frac{(\gamma+1)^2}{\gamma}\right)^{1-2/3\bar{\mu}} \right]^{-1.5}, & \\ \text{if } v_{imp} \geq v_{supercat} & \end{cases} \quad (6)$$

where μ' is the reduced mass of the target and projectile, γ is the projectile-to-target mass ratio, ρ_1 is the nominal density of 1000 kg/m^3 , and R_{C1} is the radius of a sphere of density ρ_1 and mass equal to the total mass of the system. The impact speed for the onset of super-catastrophic disruption

$v_{supercat}$ is the critical impact speed at $m_{lr} = 0.1m_{tot}$, which can be calculated by the second formula in Eq. (6). The best-fit values of the dimensionless material parameters c^* and $\bar{\mu}$ in our case are 3.0 and 0.385, respectively, which are consistent with the suggested values for small bodies in the gravity regime of Leinhardt and Stewart (2012): $c^* = 5 \pm 2$ and $\bar{\mu} = 0.37 \pm 0.1$. The good agreements imply that the low resolution used in the simulations would not affect the mass-loss behavior of a self-gravitating rubble pile in the collision. The two curves have an inflection at mass ratio ~ 0.1 , where the collision regime is converted from disruption to super-catastrophic disruption. Because the collisional remnants of super-catastrophic impacts are highly dispersed and have the highest error in N -body simulations, we limit our study to the disruption regime. On the basis of the collision tests, simulations are done with impact speeds of $0.5\text{--}30v_{esc}$ for each e .

4 Results

This section presents the collision outcomes for the rubble piles in heliocentric orbits. The dependence on the orbital phase of impact in an elliptical orbit is investigated. Furthermore, the effect of orbital eccentricity on the relation between the largest remnant mass and the impact speed is shown.

4.1 Influences of orbital phase

For a highly elliptical orbit, the amplitude of disturbing forces can vary by an order of magnitude within one orbital period (see Fig. 1). The small body has lower effective gravity to capture the escaping ejecta near perihelion (i.e., $f = 0^\circ$). As a result, mass loss will be enhanced when the impact takes place near perihelion. We conducted 200 simulations at impact speeds of 8 m/s and 12 m/s at $e = 0.5$, to survey the effect of the orbital phase (i.e., the true anomaly) at the moment of impact. The impact tests are distributed uniformly in time (not true anomaly) throughout one orbit period, so more impacts are simulated near aphelion than perihelion.

Figure 5 shows the relation between the ratio of the mass of the largest remnant to the total mass and the true anomaly f at the corresponding orbital impact position in the case of $e = 0.5$. As shown in Fig. 5, depending on the orbital phase, the normalized mass loss can vary by several percent of the total system mass (i.e., a few to tens of particles in this case). The orbital perturbations can also affect the configurations of the post-collisional fragments. The results of the impact at 8 m/s are especially consistent with the dynamical analysis, in which the largest remnant is always larger when the impact occurs near aphelion. For the impact at 12 m/s,

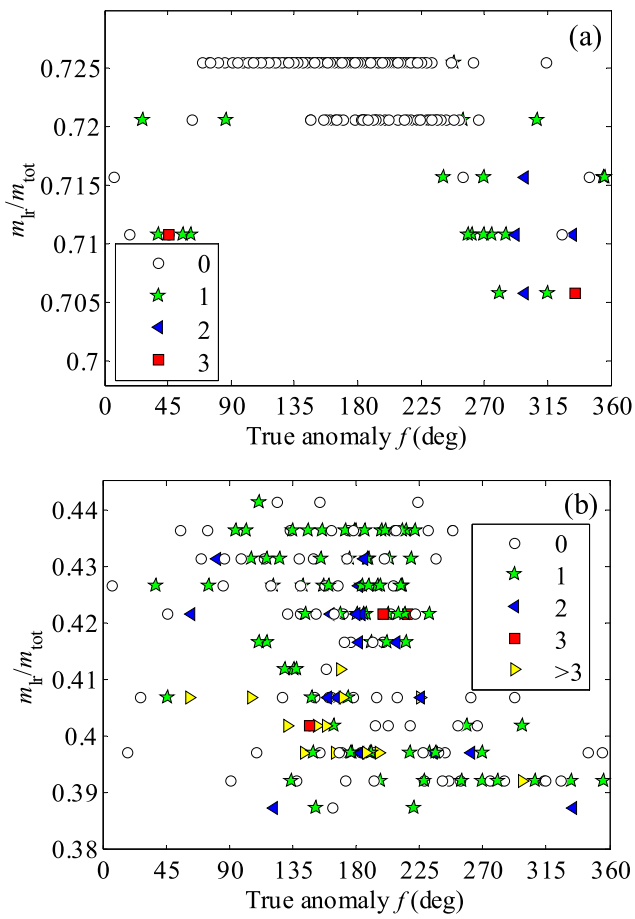


Fig. 5 Mass ratio m_{lr}/m_{tot} for $e = 0.5$ at different impact speeds: (a) 8 m/s, (b) 12 m/s. Each marker represents a simulated result for a given f , and its shape signifies the number of satellites that were trapped around the largest remnant for at least one year. An open circle denotes no satellite, a star denotes one satellite, a left-pointing triangle denotes two satellites, a square denotes three satellites, and a right-pointing triangle denotes more than three satellites

the effect of the impact position is less clear. As shown in Fig. 5b, the range of mass ratio m_{lr}/m_{tot} around aphelion, $f \in (100^\circ, 225^\circ)$, is quite wide. Note, in this case, the mass loss exceeded half of the mass of the original target, where interactions between ejected fragments become complicated and have a significant impact on the final outcome.

4.2 Influences of orbital eccentricity

Because the effect of an elliptical orbit on collision outcome is greatest at perihelion, the collision simulations for different orbital eccentricities were conducted at $f = 0^\circ$. The relation between the normalized mass of the largest remnant and the normalized impact speed is shown in Fig. 6. The mass of the largest remnant is represented as the sum of its own mass and the mass of materials gravitationally bound to it. In general, we find that the mass loss is enhanced for a larger orbital eccentricity at a given impact speed, as ex-

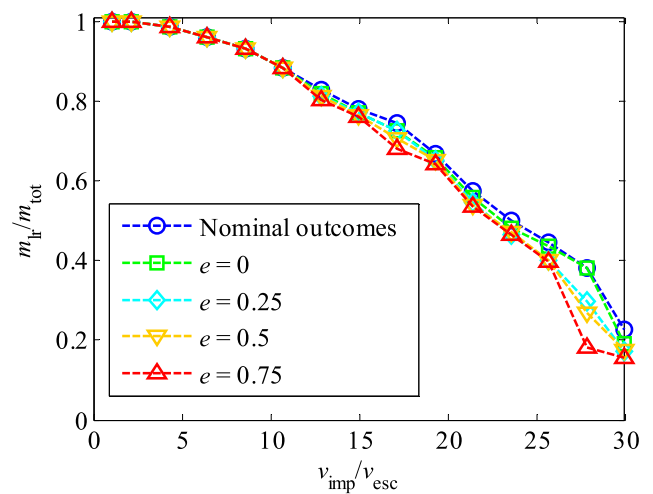


Fig. 6 Mass ratio m_{lr}/m_{tot} for different orbital eccentricities for a set of collisions. The initial orbital impact positions are set at $f = 0^\circ$ (i.e., perihelion) for all simulations. The nominal outcomes are the results of the rubble-pile model in the collision test (see Fig. 4)

pected from Eq. (2). When $v_{imp} < 10v_{esc}$, because the quantity of escaping ejecta is small, no opportunity exists for critical-ejecta generation, resulting in the invariable mass-loss outcomes for all simulations. When $v_{imp} > 10v_{esc}$, the perturbing forces influence the dynamical evolution of impact ejecta. As shown in Fig. 6, for a circular orbit, a small variation occurs in the mass of the largest remnant compared with the nominal outcomes (i.e., the simulation results without the orbital motion in Sect. 3.2). For an elliptical orbit, the perturbing forces enhance the mass loss by a few to tens of percent of the total system mass, which is similar in effect to the case of pre-impact rotation (Ballouz et al. 2014). Hence, the influence of orbital effect should be considered in investigations of collision processes.

Overall, the collision outcomes are very sensitive to the orbital phase and eccentricity of the target asteroid. As indicated in Eq. (2), the orbital phase and eccentricity affect the outcome in a similar manner, which depends on the speed of the asteroid at impact and its distance from the Sun. In the following section, we only analyze the situations of perihelion collisions with different eccentricities.

5 Discussion

From the above analyses, our simulation results indicate that orbital perturbations arising from an asteroid’s elliptical orbit can have a significant impact on the mass loss following a collisional event. In this section, we apply the catastrophic disruption threshold and the ejecta velocity distribution to estimate the degree of influence of the orbital eccentricities.

Table 2 List of catastrophic disruption thresholds

Orbit parameter	Q_{RD}^* (J/kg)
Nominal	1.22 ± 0.02
$e = 0$	1.18 ± 0.03
$e = 0.25$	1.12 ± 0.01
$e = 0.5$	1.10 ± 0.01
$e = 0.75$	1.06 ± 0.03

5.1 Catastrophic disruption threshold

In the literature on planetary and asteroid collisions (e.g., Benz and Asphaug 1999), the outcomes of impact are parameterized using a catastrophic disruption threshold, Q_D^* , which is the specific impact energy required to disperse half the total system mass. To evaluate the collision outcomes between different-size impactors, Stewart and Leinhardt (2009) considered the reduced mass μ' in a modification of the specific energy definition by introducing the reduced-mass specific impact energy $Q_R \equiv 0.5\mu'v_{imp}^2/m_{tot}$. The corresponding reduced-mass catastrophic disruption threshold is $Q_{RD}^* \equiv 0.5\mu'v_{imp}^{*2}/m_{tot}$, where v_{imp}^* is the critical impact speed required to disperse half the total system mass. Using the new variables, they found that the relation between the mass of the largest remnant and the impact energy can be described by a single linear formula:

$$m_{lr}/m_{tot} = -0.5(Q_R/Q_{RD}^*) + 1, \tag{7}$$

which they termed the “universal law” for the mass of the largest remnant.

Using a linear least-squares fit of the collision outcomes, we calculate the reduced-mass catastrophic disruption threshold for each set of orbital eccentricities in our simulations. Table 2 presents the results of the fitting. Each fitting value of Q_{RD}^* is presented with the standard deviation of each fit. The results show that the orbital eccentricity of the asteroid has an important effect on the value of Q_{RD}^* in the collisional disruption of a rubble-pile asteroid. With the increase of the orbital eccentricity, Q_{RD}^* systematically decreases by approximately 5–10 % relative to the $e = 0$ case. In addition, the value of Q_{RD}^* in the $e = 0$ case is notably smaller than that in the nominal case because of the solar tidal effect and the Coriolis effect in a circular heliocentric orbit (see Eq. (2) at $e = 0$).

Using the fitting value of Q_{RD}^* in Table 2, we plot the normalized mass of the largest remnant as a function of the normalized impact energy in Fig. 7. Our results are in good agreement with the universal law, except for several high-energy impact cases. The feature is consistent with the phenomenon observed in the results of Ballouz et al. (2015). They suggested that the target was catastrophically disrupted in such high-energy impact events, and the largest remnant

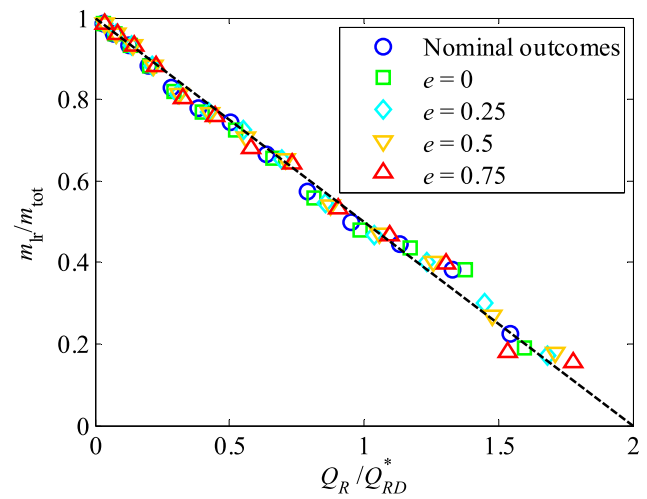


Fig. 7 Mass ratio m_{lr}/m_{tot} versus the normalized impact energy Q_R/Q_{RD}^* for all simulations. The black dashed line is the universal law for the mass of the largest remnant (Eq. (7))

became less representative of the collisional dynamics. Nevertheless, the maximum deviation in m_{lr}/m_{tot} of our results from Eq. (7) is less than 10 %. Therefore, the universal law can also be applied to describe the collision outcomes of gravitational aggregates on an elliptical heliocentric orbit.

5.2 Ejecta velocity distribution

The mass and velocity distribution of the ejecta are the main factors that determine whether collisions are erosive or accretive, and the degree of mass loss (Housen and Holsapple 2011). To characterize the source of variations in mass loss between different orbits, the ejecta velocity distributions are analyzed in this section.

In order to calculate the ejection velocity, \mathbf{v} , a reference point and a reference surface are needed. Because the rubble-pile particles are highly dispersed by the impact before forming the largest remnant, the center of mass is no longer located at the center of the largest remnant particle distribution, and no reference surface is available to calculate the ejection velocity. Therefore, we introduce a local sphere to serve as the reference system. Figure 8 shows the configurations of the local sphere and the rubble-pile particles in different stages of the simulation for an impact speed of 8 m/s. The local sphere is a hypothetical surface with a fixed radius, r_l , and it contains a non-dispersed aggregate. To obtain the ejection velocity for all the ejecta, the value of r_l should be no less than the bulk radius of the rubble pile. The non-dispersed aggregate is the largest clump of particles in the current simulated scene and eventually develops into the largest remnant (see the particles inside the local sphere in Fig. 8). The center of the local sphere is located at the center of mass of the non-dispersed aggregate and moves with it. The ejection velocity of a particle can be determined when

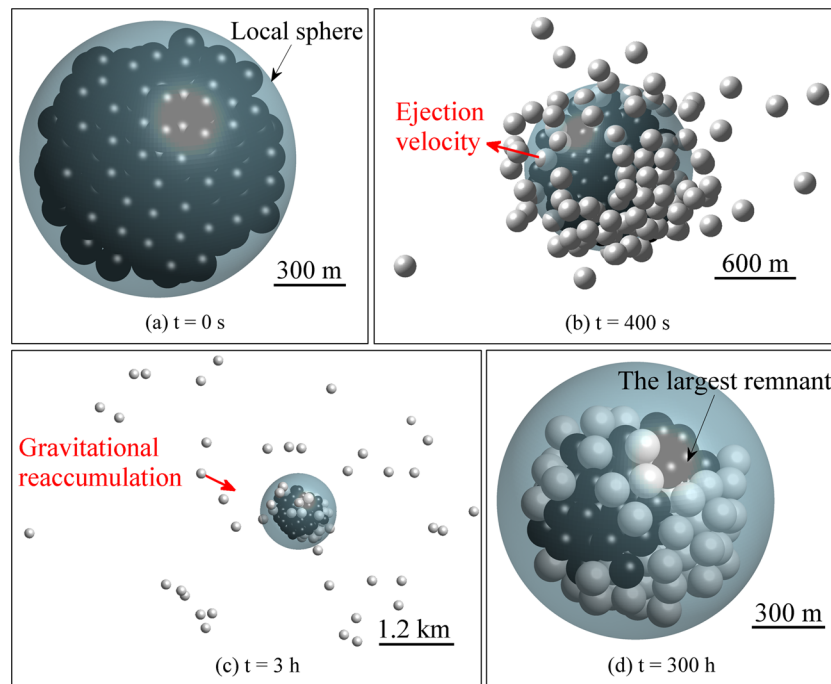


Fig. 8 Snapshots of the collision process at an impact speed of 8 m/s. The large translucent sphere is the “local sphere” and the smaller ones are the rubble-pile particles. The *gray particles* are those that have crossed or are crossing the surface of the local sphere, and the *black particles* are those that have not had a chance to leave the local sphere at the corresponding time point. These frames are presented in chrono-

logical order: (a) the initial configuration of the local sphere and the rubble-pile particles, (b) the ejection of those particles several seconds later, (c) the gravitational reaccumulation that occurs because of the slow ejection speed of some particles, and (d) the final largest fragment shown inside the local sphere, in which the *gray particles* denote the ones that were reaccumulated

it crosses through the local surface. By this means, we can acquire all the ejecta velocity information. The ejecta velocity distribution is quantified by the ratio of the total mass of material ejected with speed greater than v and the total mass, $M(v)/m_{\text{tot}}$. Figure 9 shows the $M(v)/m_{\text{tot}}$ histograms of all orbit scenarios at impact speeds of 8 m/s and 12 m/s. The radius of the local sphere, r_l , is set to the bulk radius of the target, i.e., 0.6 km. The maxima of these curves (i.e., $M(0)/m_{\text{tot}}$) are less than 1 because several particles tend to stay in the local sphere at all times (see the black particles in Fig. 8d). These particles do not cross the surface of the local sphere, and their contributions to $M(v)/m_{\text{tot}}$ are neglected.

To characterize the mass loss from the ejecta velocity distribution, the effective escape speed needs to be determined for each case. For a single spherical body, the local escape speed for a massless particle is derived simply from conservation of energy, such that the particle has zero speed at infinity. However, the situation is more complicated in the three-body problem, since the motion of the third particle around an asteroid is believed to be chaotic when the gravitational perturbation of the Sun is considered (Astakhov et al. 2003). To characterize the escape speed in this case, the infinite space is replaced with the non-escape zone. Once a particle arrives at the boundary of the zone with a non-zero speed, it can escape from the gravity of the asteroid.

Previous research shows that the zone of orbital stability around the asteroid is reduced because of the perturbations of the Sun’s gravity. By analyzing the Jacobi constant where the topology of the zero-velocity curves changes, Szebehely (1978) predicted that particles in circular orbits around asteroids will escape when the orbital radius becomes larger than $r_H/3$ (r_H is the Hill radius defined in Sect. 2.2). The numerical results of Hamilton and Burns (1991) for initially circular orbits also indicated that the radius of the stability zone is $\sim 0.49r_H$ for prograde orbits and $\sim r_H$ for retrograde orbits. Although the above research is based on the circular restricted three-body problem, the relation between the radius of the stability zones and the Hill radius can be used to infer the size of the non-escape region in the ERTBP. In this study, we assume that the radius of the non-escape zone is λr_H . The dimensionless parameter λ is a measure of how the motion of the ejecta is influenced by the perturbing forces. From this, the escape speed can be written as

$$\tilde{v}_{\text{esc}} = \sqrt{2Gm_0 \left(\frac{1}{r_l} - \frac{1}{\lambda r_H} \right)}, \quad (8)$$

where m_0 is the effective mass that exerts gravitational pull on the ejected particles. Because the mass of the non-dispersed aggregate decreases immediately after the impact (see Fig. 8b), the actual mass of materials that can provide

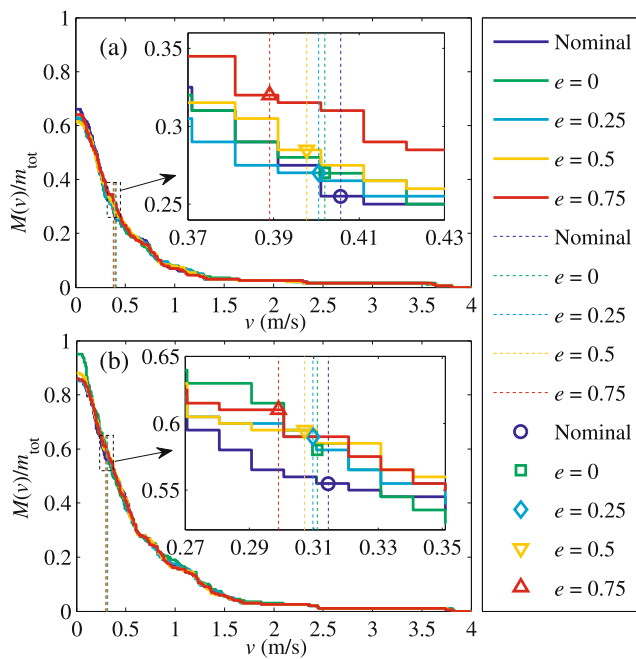


Fig. 9 Cumulative mass versus speed of fragments that exit the local sphere (solid thick lines). (a) $v_{\text{imp}} = 8$ m/s; (b) $v_{\text{imp}} = 12$ m/s. The dashed thin line defines the separatrix, the speed that separates retained from escaping ejecta. The symbol marks the corresponding mass ratio at the escape critical point for each eccentricity

effective gravity to capture the ejecta is less than the original target mass. The value of m_0 is thus generally less than the total system mass. The Hill radius is taken to the distance where the normalized solar tidal acceleration is equal to 1, which decreases with the increase of the orbital eccentricity (see Fig. 3). The influence of orbital eccentricity is mainly embodied in the Hill radius. Under given impact conditions (i.e., the impact speed in this study) and the rubble-pile model, the escape speed parameters, (m_0, λ) , are constant for all orbital eccentricities, and for the corresponding nominal case (where r_H is infinity). Therefore, the escape speed decreases with the increase of the orbital eccentricity at given conditions (see the dashed thin lines in Fig. 9 for an example). In practice, m_0 and λ are determined by fitting the mass loss in the nominal case and in the $e = 0$ case with the ejecta velocity distribution curve, respectively.

Figure 9 shows the value of escape speed for all orbit scenarios at impact speeds of 8 m/s and 12 m/s (i.e., the dashed thin lines). The value of m_0 is found to be $0.725m_{\text{tot}}$, and $0.436m_{\text{tot}}$ for the impact speeds of 8 m/s and 12 m/s, respectively, which is approximately equal to the mass of the largest remnant for each case (see Fig. 6). The value of λ is found to be 0.2 and 0.17 for the impact speeds of 8 m/s and 12 m/s, respectively. When the ejection speed of a particle exceeds \tilde{v}_{esc} , it will escape forever; otherwise, it will re-impact or orbit the largest remnant. Thus, the total mass of escaped ejecta in each case (i.e., the ordinate value of each

symbol) is actually the mass loss caused by an impact, which is consistent with the collision outcomes shown in Fig. 6.

Comparing the ejecta velocity distribution curves and the values of escape speed, two major factors are found to contribute to the variations in mass loss. First, with the increase of eccentricity, the separatrix of escape speed moves to the left in Fig. 9 because of the influence of long-term perturbations in the three-body system. This is the main cause of the increments of mass loss. The so-called critical ejecta are located between the lines of the smallest and largest effective escape speeds. Second, the ejecta velocity distribution varies with the orbital conditions. The granular system is a highly nonlinear system with a lot of factors correlated, i.e., inhomogeneous force propagation, the nonlinear contact response, and the breaking and forming of interparticle contacts. Even in the linear spring contact model, fluctuations caused by a single contact responding to an external force can spread to all vibrational modes (Schreck et al. 2011). Therefore, in our simulations, the state of motion of the particles can be affected by the orbital perturbations during collision; as a consequence, the energy and momentum coupling between colliding particles changes. In turn, the collisional interaction can also affect the motion of ejecta. These factors influence each other and eventually lead to significant variations in the ejecta velocity distribution. However, in the above simulations, we intentionally reduce some of the factors that may obscure the effect of orbital perturbations, such as the amount of dissipation. In the next section, a more realistic model is applied to estimate the effect of these complicating factors.

6 Implications for collisional disruption

Although very little is known about the actual mechanical properties of asteroid material, the contact interaction between the constituent particles cannot be frictionless. By comparing numerical simulations with avalanche experiments using roughly equal-size rocks collected from a streambed, Yu et al. (2014) found a set of soft-sphere parameters (the “gravel” parameters) that can appropriately reflect the typical behavior of the rocks (“gravel” in Table 1). The high coefficients of friction reflect the irregular non-spherical shapes of actual granular matter. While the actual relation of the granular interactions on Earth to those on the small bodies is unclear, the gravel model can serve as a reasonable surrogate until more data are available. To gain more insight into the orbital effect on collision outcomes, we carry out a series of numerical simulations using the smooth and gravel parameters with higher resolution, $N_{\text{targ}} = 2896$. Two internal configurations of rubble pile model with different macroporosities are considered. Using the method introduced in Sect. 3.1, the normal spring constant k_n is set to

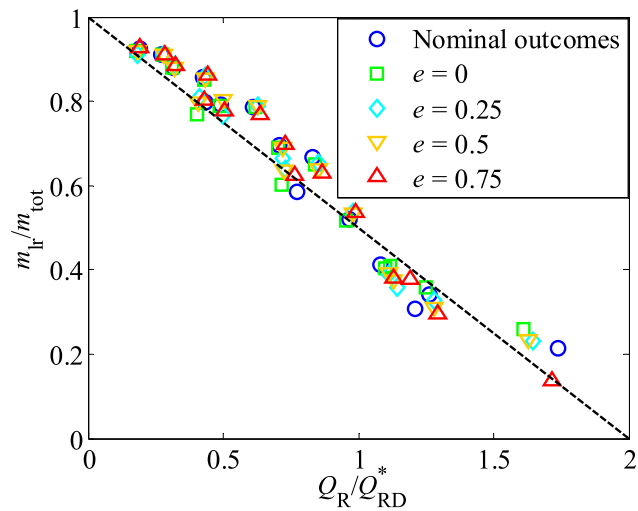


Fig. 10 Mass ratio m_{lr}/m_{tot} versus the normalized impact energy Q_R/Q_{RD}^* for the high-resolution model. The *black dashed line* is the universal law for the mass of the largest remnant (Eq. (7))

$\sim 1.53 \times 10^{12} \text{ kg/s}^2$ and the timestep Δt is set to ~ 4 ms, ensuring that particle overlaps do not exceed much more than 1 % of the particle radii. The amount of mass loss is determined by measuring the total mass of all material that is gravitationally bound to the instantaneous largest remnant. The simulation runs until the measured amount of mass loss achieves a steady value (this requires about 20 system dynamical times). The mass loss outcomes of each simulation are summarized in Table 3. Following the analyses in the low-resolution model, we calculate the reduced-mass catastrophic disruption threshold and characterize the escape speed parameters, (m_0, λ) , from the ejecta velocity distribution (to reduce the influence of particle-particle collisions on the calculation of ejection velocity, the radius of the local sphere is set to 0.8 km) for each set of simulations (Table 3), and compare the results to the universal law (Fig. 10).

As shown in Table 3 and Fig. 10, the orbital perturbations still have significant effects on the collision outcomes and the value of Q_{RD}^* . The universal law can also be applied to describe the collision outcomes in these cases. However, comparing with the results of the low-resolution model (i.e., Fig. 6), the trend that the mass loss will increase with the larger orbital eccentricity is not obvious, especially for the high-porosity “gravel” material set of simulations. According to the analyses in Sect. 2, mass-loss enhancement due to the orbital perturbations is expected to happen since the solar tidal force and the Coriolis force will weaken the gravitational pull of the asteroid. However, the perturbation theory and the “critical ejecta” theory are both based on the assumption that the position and velocity distribution of post-collision fragments are nearly constant. Figure 11 shows the $M(v)/m_{tot}$ histograms at different impact speeds with

similar mass losses for the three high-resolution models. It is clear to see that the ejecta velocity distribution changes significantly with the orbit eccentricity, which becomes the main cause of the variations in mass loss compared to the effect of the change in the escape speed.

Through tracking the contact networks during collisions, we find that the phase of most intensive interparticle collisions occurs at the beginning of impact and lasts for a few minutes. After that, the total contact number decreases until fragments start to reaccumulate. In order to isolate the complexity due to the interparticle collisions, a set of simulations at an impact speed of 10 m/s with the low-porosity “gravel” model is conducted by using the output after the phase of intensive collisions (i.e., the output at the simulation time of 400 s) in the nominal cases as the initial conditions for all orbit cases (henceforth, the “post-collision” experiment). Figure 11(d) shows the ejecta velocity distribution for the “post-collision” experiment, where the escape velocity parameters are the same as those of the low-porosity “gravel” material set of collisions at $v_{imp} = 10$ m/s. In this case, the ejecta velocity distribution curve is almost constant for all orbital conditions. It is also worth noting that the variation of mass loss in the “post-collision” experiment (~ 0.014) is much smaller than in the corresponding normal case (i.e., Fig. 11(b), where the variation is ~ 0.027). This implies that the orbital perturbations can exert an indirect significant influence on the velocity field of post-ejection fragments through interparticle collisions.

Although the orbit dependence of mass loss in collisions is ambiguous for the high-resolution model, comparing the value of the catastrophic disruption threshold shows that Q_{RD}^* , which represents the capacity of the asteroid structure to resist disruption, systematically decreases with the increase of the orbital eccentricity, except for the high-porosity “gravel” material set of collisions. Furthermore, the variation in mass loss for different orbital conditions is larger when a coarse material model or high-porosity model is used. This indicates that the orbital perturbations have a stronger effect on the velocity field of post-collision fragments in these cases.

These differences can be explained by analyzing the propagation of the shock wave. During a collision, a shock wave travels through the target, transfers the momentum into the constituent particles, and results in disruption of the gravitational aggregates. The macroscopic porosity, which is an inherent property of the rubble-pile model, causes reflections when the shock wave encounters a void (Jutzi and Michel 2014). In other words, it will take longer for the shock wave to propagate throughout the rubble piles with higher macroporosity. Therefore, the orbital perturbations have more time to affect the force distribution network in the rubble pile and cause significant changes in the ejection velocity of each particle. Furthermore, the propagation

Table 3 Summary of collision conditions and mass loss outcomes ($N_{\text{targ}} = 2896$)

Orbit parameter	Material	Macroporosity	v_{imp} (m/s)	$m_{\text{lr}}/m_{\text{tot}}$	Q_{RD}^* (J/kg)	m_0/m_{tot}	λ	$m_{\text{lr}}/m_{\text{tot}}$ predicted
Nominal	Smooth	48.7 %	4	0.911	0.568	0.948	1.00 ^a	0.911 ^b
Nominal	Smooth	48.7 %	5	0.856		0.910	1.00	0.856
Nominal	Smooth	48.7 %	6	0.785		0.868	1.00	0.785
Nominal	Smooth	48.7 %	7	0.666		0.759	0.35	0.666
Nominal	Smooth	48.7 %	8	0.411		0.621	1.00	0.411
$e = 0$	Smooth	48.7 %	4	0.910	0.560	0.948	1.00	0.910
$e = 0$	Smooth	48.7 %	5	0.851		0.910	1.00	0.851
$e = 0$	Smooth	48.7 %	6	0.786		0.868	1.00	0.785 ^c
$e = 0$	Smooth	48.7 %	7	0.651		0.759	0.35	0.651
$e = 0$	Smooth	48.7 %	8	0.403		0.621	1.00	0.367
$e = 0.25$	Smooth	48.7 %	4	0.911	0.553	0.948	1.00	0.911
$e = 0.25$	Smooth	48.7 %	5	0.860		0.910	1.00	0.860
$e = 0.25$	Smooth	48.7 %	6	0.790		0.868	1.00	0.794
$e = 0.25$	Smooth	48.7 %	7	0.652		0.759	0.35	0.656
$e = 0.25$	Smooth	48.7 %	8	0.389		0.621	1.00	0.398
$e = 0.5$	Smooth	48.7 %	4	0.911	0.552	0.948	1.00	0.911
$e = 0.5$	Smooth	48.7 %	5	0.853		0.910	1.00	0.852
$e = 0.5$	Smooth	48.7 %	6	0.788		0.868	1.00	0.786
$e = 0.5$	Smooth	48.7 %	7	0.639		0.759	0.35	0.645
$e = 0.5$	Smooth	48.7 %	8	0.393		0.621	1.00	0.403
$e = 0.75$	Smooth	48.7 %	4	0.911	0.544	0.948	1.00	0.911
$e = 0.75$	Smooth	48.7 %	5	0.863		0.910	1.00	0.861
$e = 0.75$	Smooth	48.7 %	6	0.768		0.868	1.00	0.771
$e = 0.75$	Smooth	48.7 %	7	0.631		0.759	0.35	0.634
$e = 0.75$	Smooth	48.7 %	8	0.382		0.621	1.00	0.407
Nominal	Gravel	48.7 %	8	0.879	1.952	0.904	1.00	0.879
Nominal	Gravel	48.7 %	10	0.791		0.891	0.25	0.791
Nominal	Gravel	48.7 %	12	0.695		0.743	0.40	0.695
Nominal	Gravel	48.7 %	14	0.521		0.554	1.00	0.521
Nominal	Gravel	48.7 %	16	0.340		0.382	0.10	0.340
$e = 0$	Gravel	48.7 %	8	0.881	1.973	0.904	1.00	0.880
$e = 0$	Gravel	48.7 %	10	0.789		0.891	0.25	0.789
$e = 0$	Gravel	48.7 %	12	0.690		0.743	0.40	0.690
$e = 0$	Gravel	48.7 %	14	0.516		0.554	1.00	0.515
$e = 0$	Gravel	48.7 %	16	0.359		0.382	0.10	0.359
$e = 0.25$	Gravel	48.7 %	8	0.885	1.923	0.904	1.00	0.883
$e = 0.25$	Gravel	48.7 %	10	0.767		0.891	0.25	0.770
$e = 0.25$	Gravel	48.7 %	12	0.665		0.743	0.40	0.668
$e = 0.25$	Gravel	48.7 %	14	0.537		0.554	1.00	0.548
$e = 0.25$	Gravel	48.7 %	16	0.327		0.382	0.10	0.313
$e = 0.5$	Gravel	48.7 %	8	0.879	1.920	0.904	1.00	0.879
$e = 0.5$	Gravel	48.7 %	10	0.802		0.891	0.25	0.798
$e = 0.5$	Gravel	48.7 %	12	0.689		0.743	0.40	0.691
$e = 0.5$	Gravel	48.7 %	14	0.534		0.554	1.00	0.538
$e = 0.5$	Gravel	48.7 %	16	0.310		0.382	0.10	0.335

Table 3 (Continued)

Orbit parameter	Material	Macroporosity	v_{imp} (m/s)	$m_{\text{lr}}/m_{\text{tot}}$	Q_{RD}^* (J/kg)	m_0/m_{tot}	λ	$m_{\text{lr}}/m_{\text{tot}}$ predicted
$e = 0.75$	Gravel	48.7 %	8	0.884	1.901	0.904	1.00	0.880
$e = 0.75$	Gravel	48.7 %	10	0.777		0.891	0.25	0.772
$e = 0.75$	Gravel	48.7 %	12	0.697		0.743	0.40	0.690
$e = 0.75$	Gravel	48.7 %	14	0.538		0.554	1.00	0.531
$e = 0.75$	Gravel	48.7 %	16	0.297		0.382	0.10	0.205
Nominal	Gravel	60.9 %	8	0.925	3.185	0.990	1.00	0.925
Nominal	Gravel	60.9 %	12	0.798		0.869	0.20	0.798
Nominal	Gravel	60.9 %	16	0.585		0.611	1.00	0.585
Nominal	Gravel	60.9 %	20	0.308		0.444	1.00	0.308
Nominal	Gravel	60.9 %	24	0.215		0.418	1.00	0.215
$e = 0$	Gravel	60.9 %	8	0.919	3.442	0.990	1.00	0.919
$e = 0$	Gravel	60.9 %	12	0.770		0.869	0.20	0.770
$e = 0$	Gravel	60.9 %	16	0.602		0.611	1.00	0.600
$e = 0$	Gravel	60.9 %	20	0.409		0.444	1.00	0.383
$e = 0$	Gravel	60.9 %	24	0.260		0.418	1.00	0.252
$e = 0.25$	Gravel	60.9 %	8	0.912	3.365	0.990	1.00	0.914
$e = 0.25$	Gravel	60.9 %	12	0.809		0.869	0.20	0.802
$e = 0.25$	Gravel	60.9 %	16	0.638		0.611	1.00	0.619
$e = 0.25$	Gravel	60.9 %	20	0.357		0.444	1.00	0.358
$e = 0.25$	Gravel	60.9 %	24	0.230		0.418	1.00	0.195
$e = 0.5$	Gravel	60.9 %	8	0.918	3.401	0.990	1.00	0.918
$e = 0.5$	Gravel	60.9 %	12	0.798		0.869	0.20	0.791
$e = 0.5$	Gravel	60.9 %	16	0.637		0.611	1.00	0.618
$e = 0.5$	Gravel	60.9 %	20	0.376		0.444	1.00	0.379
$e = 0.5$	Gravel	60.9 %	24	0.234		0.418	1.00	0.216
$e = 0.75$	Gravel	60.9 %	8	0.927	3.224	0.990	1.00	0.925
$e = 0.75$	Gravel	60.9 %	12	0.804		0.869	0.20	0.787
$e = 0.75$	Gravel	60.9 %	16	0.625		0.611	1.00	0.609
$e = 0.75$	Gravel	60.9 %	20	0.379		0.444	1.00	0.368
$e = 0.75$	Gravel	60.9 %	24	0.136		0.418	1.00	0.104

m_0/m_{tot} —artificial mass parameter normalized by total mass, which is determined by fitting the mass loss with the escape speed (Eq. (8)) and the ejecta velocity distribution curve in the corresponding nominal case; λ —radius of the stability zone in r_H ranging from 0 to 1, which is determined by fitting the mass loss in the case of $e = 0$ based on the corresponding value of m_0 ; $m_{\text{lr}}/m_{\text{tot}}$ predicted—the mass of the largest remnant deduced from the escape speeds and the ejecta velocity distribution curves

^aThe escape speed parameters, (m_0 , λ), are constant for all the orbit scenarios under the given impact speed and rubble-pile model

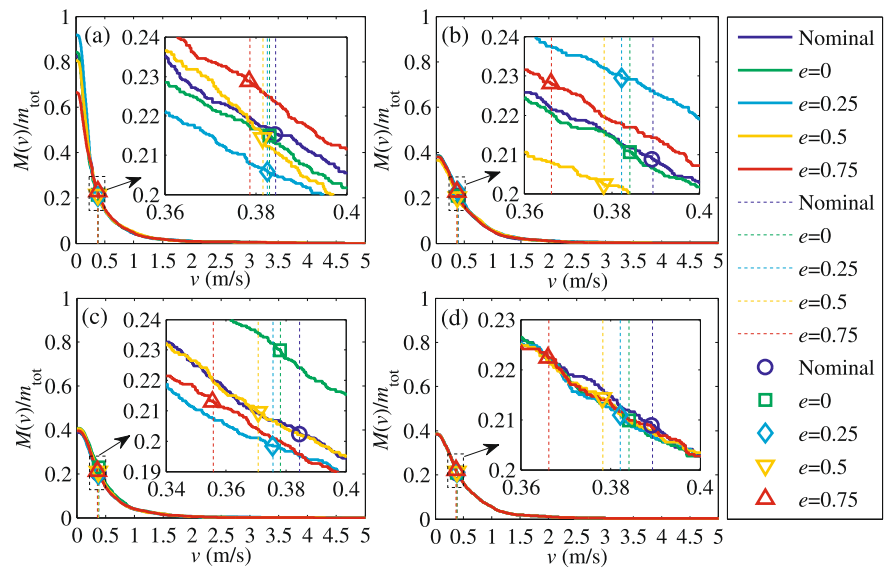
^bPredicted $m_{\text{lr}}/m_{\text{tot}}$ in all nominal cases is the same as the simulation result

^cPredicted $m_{\text{lr}}/m_{\text{tot}}$ in the $e = 0$ cases may be slightly less than the simulation result, because the value of λ has an upper bound of 1

of the shock wave also depends on several physical properties, such as the strain loading and unloading rate and the material parameters (Ballouz et al. 2015). In the SSDEM model (Schwartz et al. 2012), the friction forces are sensitive to the surface velocity of the colliding particles. When a set of high friction coefficients (i.e., the “gravel” parameters) is used in simulations, a slight change in the veloc-

ity field due to the orbital perturbations will lead to significant changes in the force chains of the aggregate, which will in turn affect the velocity of the ejected particles. As a consequence, the influence of the orbital perturbations on the position and velocity distribution of post-collision fragments is enhanced in the “gravel” material set of collisions.

Fig. 11 Cumulative mass versus speed of fragments that exit the local sphere for the high-resolution model. (a) $v_{\text{imp}} = 6$ m/s with the “smooth” material set of collisions; (b) $v_{\text{imp}} = 10$ m/s with the low-porosity “gravel” material set of collisions; (c) $v_{\text{imp}} = 12$ m/s with the high-porosity “gravel” material set of collisions; (d) the “post-collision” experiment. The shape and style of the symbols and lines are the same as in Fig. 9



It is also worth noting that the combination of ejecta velocity distributions and escape speeds can predict the value of mass loss and its dependence on orbital eccentricity quite well, except for several high-impact-speed cases where gravitational interactions between ejected fragments become complicated and have a significant impact on the final outcome (Table 3). The definition of escape speed (Eq. (8)) is a good approximation of the actual escape speed in a three-body system. Using this approach, the collision outcomes can be applied to infer the properties of the non-escape zone around asteroids in the general elliptic three-body system.

7 Conclusions and future work

Collisions between small bodies play a crucial role in the origin and evolution of the Solar System. Studying the effects that contribute to variations in the mass of small bodies is of benefit to understanding the collisional evolution models of the early Solar System. In this study, we investigated the effect of perturbing forces in elliptical orbits on the collision outcomes of a rubble-pile asteroid.

Using the linearized equation of motion in the non-uniformly rotating coordinate system of the ERTBP, we characterized the perturbing force acting on the third massless body around the asteroid. According to the analyses, the gravitational influence of the asteroid will be weakened by the solar tidal force and the Coriolis effect. Moreover, the magnitude of these perturbative effects will increase with the orbital eccentricity of the asteroid, especially near perihelion. As a result, the energy of the ejecta is increased, and it will eventually escape from the gravity of the asteroid.

Our N -body collision simulations confirm that the orbital perturbations have significant effects on the mass-loss

outcomes in collision events. For the low-resolution model, with increasing orbital eccentricity, the mass ratio $m_{\text{lr}}/m_{\text{tot}}$ systematically decreases by approximately a few to tens of percent relative to the $e = 0$ case. In addition, the value of $m_{\text{lr}}/m_{\text{tot}}$ in the $e = 0$ case is slightly smaller than that in the nominal case because of the solar tidal effect and the Coriolis effect in a circular heliocentric orbit. The reduced-mass catastrophic disruption threshold Q_{RD}^* also decreases with the growth of perturbations. However, the effect of mass-loss enhancement due to the orbital perturbations is less apparent in the high-resolution simulations, especially when a set of high-friction material parameters and high-porosity structure are used.

We explained our results from the perspective of ejecta velocity distributions. By introducing a dimensionless constant λ and a mass constant m_0 , we developed an analytical description of escape velocity from the surface of the asteroid in the ERTBP. By analyzing the ejecta velocity distribution curves and the values of escape velocity, we found that the variation in mass loss is attributed to the long-term perturbations in the elliptic three-body system, and the changes in ejection velocity of post-collision fragments. The former always result in the mass loss increasing with the growth of orbital perturbations, while the effect of the latter is more complicated. In the low-resolution case, particle-particle collisions are infrequent, so the long-term perturbative effect becomes the main factor that determines the number of escaped ejected particles. Therefore, mass loss increases with increase of orbital eccentricity. However, in the high-resolution case, the influence of the orbital perturbations is mainly reflected in the particle-particle collisions, which largely offsets the effect of long-term perturbations.

Furthermore, our analyses indicate that the collision outcomes can be used to infer the properties of the non-escape

zone around asteroids in the general elliptic three-body system. Our work provides a new perspective to investigate the ejecta motion in the presence of the Sun's gravity and its effects on collision outcome. Our results also confirm that the "universal law" of catastrophic disruption derived by Stewart and Leinhardt (2009) can be applied to describe the collision outcomes of asteroids on elliptical heliocentric orbits.

Overall, we find the influence of the orbital eccentricity and phase should be considered in investigations of collision processes. This work will help inform future asteroid impact deflection missions by giving a qualitative prescription for collision outcomes in elliptical orbits. For present-day asteroid collisions, where the impact speed typically exceeds 1 km/s, the structure of the asteroid undergoes irreversible shock damage (Jutzi and Michel 2014). There are two important phases in high-speed collisions, i.e., the shock fragmentation phase and the gravitational reaccumulation phase, which have very different dynamical times (Michel et al. 2004). The time scale for the fragmentation phase can be determined by dividing the target size by the speed of sound, e.g., tenths of a second for a km-sized rocky target (Asphaug et al. 1998). After that, the fragments produced by the impact collide with each other before departing from the instantaneous largest remnant. This collision-intensive process will last several to tens of minutes (Leinhardt and Stewart 2009). During this period, the orbital perturbations can exert an influence on the velocity field of the fragments. That is, the post-ejection fragments will have a change in orbit energy and angular momentum due to the orbital perturbative effects. Therefore, although our model is restricted to low-speed impacts (<100 m/s), we argue that the results are applicable to high-speed impacts. To check this, a combination of a shock physics model and the N -body model must be applied. Also, when considering the effect of the heliocentric orbit of an asteroid, solar radiation pressure may rival the Sun's gravity in some situations, for small particles (Husmann et al. 2012). These are areas for possible future study.

Acknowledgements This research was supported by the National Basic Research Program of China (973 Program, 2012CB720000) and National Natural Science Foundation of China (NO. 11572166).

References

- Asphaug, E., Ostro, S.J., Hudson, R.S., Scheeres, D.J., Benz, W.: Disruption of kilometre-sized asteroids by energetic collisions. *Nature* **393**(6684), 437–440 (1998)
- Astakhov, S.A., Burbanks, A.D., Wiggins, S., Farrelly, D.: Chaos-assisted capture of irregular moons. *Nature* **423**(6937), 264–267 (2003)
- Ballouz, R.-L., Richardson, D.C., Michel, P., Schwartz, S.R.: Rotation-dependent catastrophic disruption of gravitational aggregates. *Astrophys. J.* **789**(2), 158 (2014)
- Ballouz, R.-L., Richardson, D.C., Michel, P., Schwartz, S.R., Yu, Y.: Numerical simulations of collisional disruption of rotating gravitational aggregates: dependence on material properties. *Planet. Space Sci.* **107**, 29–35 (2015)
- Benz, W., Asphaug, E.: Catastrophic disruptions revisited. *Icarus* **142**(1), 5–20 (1999)
- Bottke, W.F. Jr, Morbidelli, A., Jedicke, R., Petit, J.M., Levison, H.F., Michel, P., Metcalfe, T.S.: Debiased orbital and absolute magnitude distribution of the near-Earth objects. *Icarus* **156**(2), 399–433 (2002)
- Cundall, P.A., Strack, O.D.L.: A discrete numerical model for granular assemblies. *Geotechnique* **29**(1), 47–65 (1979)
- Durda, D.D., Bottke, W.F. Jr., Enke, B.L., Merline, W.J., Asphaug, E., Richardson, D.C., Leinhardt, Z.M.: The formation of asteroid satellites in large impacts: results from numerical simulations. *Icarus* **170**(1), 243–257 (2004)
- Durda, D.D., Movshovitz, N., Richardson, D.C., Asphaug, E., Morgan, A., Rawlings, A.R., Vest, C.: Experimental determination of the coefficient of restitution for meter-scale granite spheres. *Icarus* **211**(1), 849–855 (2011)
- Gong, S., Li, J.: Solar sail periodic orbits in the elliptic restricted three-body problem. *Celest. Mech. Dyn. Astron.* **121**(2), 121–137 (2015)
- Hamilton, D.P., Burns, J.A.: Orbital stability zones about asteroids. *Icarus* **92**(1), 118–131 (1991)
- Hamilton, D.P., Burns, J.A.: Orbital stability zones about asteroids. II. The destabilizing effects of eccentric orbits and of solar radiation. *Icarus* **96**(1), 43–64 (1992)
- Housen, K.R., Holsapple, K.A.: Ejecta from impact craters. *Icarus* **211**(1), 856–875 (2011)
- Husmann, H., Oberst, J., Wickhusen, K., Shi, X., Damme, F., Lüdicke, F., Lupovka, V., Bauer, S.: Stability and evolution of orbits around the binary asteroid 175706 (1996 FG3): implications for the MarcoPolo-R mission. *Planet. Space Sci.* **70**(1), 102–113 (2012)
- Jedicke, R., Metcalfe, T.S.: The orbital and absolute magnitude distributions of main belt asteroids. *Icarus* **131**(2), 245–260 (1998)
- Jewitt, D., Agarwal, J., Li, J., Weaver, H., Mutchler, M., Larson, S.: Disintegrating asteroid P/2013 R3. *Astrophys. J. Lett.* **784**(1), L8–L12 (2014)
- Jutzi, M., Michel, P.: Hypervelocity impacts on asteroids and momentum transfer. I. Numerical simulations using porous targets. *Icarus* **229**, 247–253 (2014)
- Leinhardt, Z.M., Richardson, D.C., Quinn, T.: Direct N -body simulations of rubble pile collisions. *Icarus* **146**(1), 133–151 (2000)
- Leinhardt, Z.M., Stewart, S.T.: Full numerical simulations of catastrophic small body collisions. *Icarus* **199**(2), 542–559 (2009)
- Leinhardt, Z.M., Stewart, S.T.: Collisions between gravity-dominated bodies. I. Outcome regimes and scaling laws. *Astrophys. J.* **745**(1), 79 (2012)
- Lissauer, J.J.: Planet formation. *Annu. Rev. Astron. Astrophys.* **31**, 129–174 (1993)
- Makó, Z., SzeKovits, F.: Capture in the circular and elliptic restricted three-body problem. *Celest. Mech. Dyn. Astron.* **90**(1–2), 51–58 (2004)
- Michel, P., Benz, W., Richardson, D.C.: Catastrophic disruption of asteroids and family formation: a review of numerical simulations including both fragmentation and gravitational reaccumulations. *Planet. Space Sci.* **52**(12), 1109–1117 (2004)
- Pravec, P., Harris, A.W., Michalowski, T.: Asteroid rotations. In: Bottke, W.F. Jr., Cellino, A., Paolicchi, P., Binzel, R.P. (eds.) *Asteroids III*, pp. 113–122. Univ. of Arizona Press, Tucson (2002)
- Richardson, D.C., Quinn, T., Stadel, J., Lake, G.: Direct large-scale N -body simulations of planetesimal dynamics. *Icarus* **143**(1), 45–59 (2000)
- Richardson, D.C., Leinhardt, Z.M., Melosh, H.J., Bottke, W.F. Jr., Asphaug, E.: Gravitational aggregates: evidence and evolution. In:

- Asteroids III, pp. 501–515. University of Arizona Press, Tucson (2002)
- Richardson, D.C., Walsh, K., Murdoch, N., Michel, P.: Numerical simulations of granular dynamics. I. Hard-sphere discrete element method and tests. *Icarus* **212**(1), 427–437 (2011)
- Richter, K., Keller, H.U.: On the stability of dust particle orbits around cometary nuclei. *Icarus* **114**(2), 355–371 (1995)
- Sanchez, J.P., Colombo, C., Vasile, M., Radice, G.: Multicriteria comparison among several mitigation strategies for dangerous near-earth objects. *J. Guid. Control Dyn.* **32**(1), 121–142 (2009)
- Sánchez, P., Scheeres, D.J.: Simulating asteroid rubble piles with a self-gravitating soft-sphere distinct element method model. *Astrophys. J.* **727**(2), 120 (2011)
- Schreck, C.F., Bertrand, T., O’Hern, C.S., Shattuck, M.D.: Repulsive contact interactions make jammed particulate systems inherently nonharmonic. *Phys. Rev. Lett.* **107**(7), 078301 (2011)
- Schwartz, S.R., Richardson, D.C., Michel, P.: An implementation of the soft-sphere discrete element method in a high-performance parallel gravity tree-code. *Granul. Matter* **14**(3), 363–380 (2012)
- Schwartz, S.R., Michel, P., Richardson, D.C., Yano, H.: Low-speed impact simulations into regolith in support of asteroid sampling mechanism design. I. Comparison with 1-g experiments. *Planet. Space Sci.* **103**, 174–183 (2014)
- Stadel, J.G.: Cosmological N-body simulations and their analysis, Ph.D. thesis, University of Washington (2001)
- Stewart, S.T., Leinhardt, Z.M.: Velocity-dependent catastrophic disruption criteria for planetesimals. *Astrophys. J. Lett.* **691**(2), L133–L137 (2009)
- Szebehely, V.: Stability of artificial and natural satellites. *Celest. Mech. Dyn. Astron.* **18**(4), 383–389 (1978)
- Voyatzis, G., Gkolias, I., Varvoglis, H.: The dynamics of the elliptic Hill problem: periodic orbits and stability regions. *Celest. Mech. Dyn. Astron.* **113**(1), 125–139 (2012)
- Walsh, K.J., Richardson, D.C.: Binary near-Earth asteroid formation: rubble pile model of tidal disruptions. *Icarus* **180**(1), 201–216 (2006)
- Yu, Y., Richardson, D.C., Michel, P., Schwartz, S.R., Ballouz, R.-L.: Numerical predictions of surface effects during the 2029 close approach of asteroid 99942 Apophis. *Icarus* **242**, 82–96 (2014)